

Research Article

Dynamic Modeling and Robust Control by ADRC of Grid-Connected Hybrid PV-Wind Energy Conversion System

Imad Aboudrar , Soumia El Hani, Mohamed Saleck Heyine, and Nisrine Naseri 

Energy Optimization, Diagnosis and Control, Centre de Recherche en Sciences et Techniques de l'Ingénieur et de la Santé, ENSET, Mohammed V University, Rabat, Morocco

Correspondence should be addressed to Imad Aboudrar; imad.aboudrar@um5s.net.ma

Received 19 June 2019; Accepted 13 September 2019; Published 20 October 2019

Academic Editor: Antonino Laudani

Copyright © 2019 Imad Aboudrar et al. This is an open access article distributed under the Creative Commons Attribution License, which permits unrestricted use, distribution, and reproduction in any medium, provided the original work is properly cited.

This work presents linear and nonlinear control strategies applied to a grid-connected multiple-source renewable energy system (wind and photovoltaic), in order to extract the maximum power and to enhance the control of the active and reactive powers. A new robust control strategy known as the active disturbance rejection control (ADRC) is proposed and applied to the hybrid renewable energy system (HRES), and it is based on the extended state observer (ESO) which allows us to estimate the internal and external disturbances such as modeling errors and parameter variations. The studied system consists of two conversion chains which are linked via a common DC bus and interconnected to the grid through a voltage source inverter (VSI); the first chain consists of a PV system and a DC-DC boost converter, and the second chain consists of a direct-driven wind turbine, permanent magnetic synchronous generator (PMSG), and of a AC/DC rectifier converter. The extraction of maximum power from the PV system and the wind energy conversion system is ensured by using the voltage based perturb and observe (VPO) and the optimal torque control (OTC) MPPT techniques, respectively. The ADRC technique is utilized to control the active and reactive powers by acting on the grid currents. In order to verify and validate the effectiveness of the proposed control strategy, a detailed model of the studied system is designed and evaluated under the MATLAB/Simulink software. The simulation results prove the effectiveness of the MPPT techniques in terms of maximum power extraction during the variation in the environmental conditions. Additionally, the regulation of active and reactive powers is ensured by ADRC, and the system is operating at a unity power factor. Moreover, it is demonstrated that the suggested strategy is efficient in terms of fast tracking and robustness to internal and external disturbances compared to the classical PI controller.

1. Introduction

Since the beginning of the century, global energy consumption has been growing very strongly in all regions of the world. It seems that, on a trend basis, energy consumption will continue to increase, driven by economic growth on the one hand and by the increase in per capita electricity consumption on the other hand, regardless of the scenarios considered [1]. For this reason, renewable energies appear today and in the long term as the solution that covers this energy requirement by reducing the major disadvantages of fossil fuels such as greenhouse emissions [2]. They have become an essential form of energy due to their flexibility, simplicity, use, and the multiplicity of fields

of activity in which they are called upon to play a role. These modes of production, as well as the associated means of distribution, are subject to deep changes over the next few decades [3].

Available in quantities greater than humanity's current energy needs, the resources of renewable energy also represent an opportunity for more than two billion people, living in remote areas, to have access to electricity. However, these renewable energy sources have a drawback that their output characteristic change becomes extreme because it significantly depends on climatic conditions, as solar irradiance and temperature in PV systems and wind speed in the wind turbines [4]. Consequently for better operation of these systems, maximum power point tracking (MPPT)

algorithms are needed to improve the energy efficiency of both PV and wind systems. In this context, several research has been conducted in the literature, going from the utilization of classical algorithms such as perturb and observe (PO), incremental conductance (INC), and hill climbing search (HCS) [5, 6] for both PV and WECS applications, to those based on artificial intelligence as fuzzy logic and neural networks [7].

The grid-side converter is a necessary element in an electrical power generation system for obtaining sinusoidal waveforms with low total harmonic distortion. Nevertheless, the performance of the system depends largely on the control strategy applied by the grid-side converter [8]. Therefore, several control techniques for the voltage inverter have been discussed in the literature. Among them, in [9], the authors deal with a new nonlinear backstepping sliding mode control for photovoltaic- (PV-) based grid interactive voltage source converter (VSC) system, and a new small signal stability phenomenon is depicted by the multivariable dynamic model of the proposed PV-based grid converter system, where PV penetration as well as nonlinear control parameter optimization practices is considered in this paper. In [10], the authors presented different topologies and control strategies for grid-connected photovoltaic systems, and the following sections report, investigate, and present control structures for single-phase and three-phase inverters. Some solutions to control the power injected into the grid and functional structures of each configuration are proposed. Jain et al. in [11] presented a review for the control strategies applied to the grid-connected PMSG-based wind turbines, a comparative study of rotor flux-oriented control and direct torque control (DTC) techniques applied in the generator-side converter of PMSG wind turbine application, for grid-side converter, and various control schemes are developed mainly based on voltage-oriented control (VOC) or on direct power control (DPC). And authors in [12] have presented a sensorless maximum power point tracking (MPPT) method for a hybrid photovoltaic-wind system, which consists of photovoltaic (PV) system and doubly fed induction generator (DFIG) wind turbine (WT). The performance of the proposed method is demonstrated in the simulation study, and the three converters can work very well to handle the power flow under various operation scenarios, such as variations of mechanical power and irradiation, changes of DC-link voltage. Hence, the proposed system can be a cost-effective alternative of the two separated systems.

In general, the most commonly used control strategy to connect the power generation systems with the utility power grid is based on the proportional integrator controller due to its simple structure as presented in [13, 14]. Considering the internal and external disturbances of grid-connected multiple-source renewable energy systems such as a hybrid PV-wind system, the control objective becomes more difficult and ordinary controllers like PI and PR controllers are not sufficient. Therefore, several researchers have proposed and investigated nonlinear controllers to drive this system as in

[15]. A control strategy based on the sliding mode control theory is proposed for the hybrid grid-connected PV-wind system where the obtained results are satisfactory and, nevertheless, this controller presents oscillations around its references due to the chattering phenomena. In [16], the authors have designed a backstepping controller for PV-wind hybrid system with grid interfacing and shunt active filtering functionality, but to ensure stability or the negativity of the derivative of the every-step Lyapunov function, it usually requires the cancellation of the indefinite cross-coupling terms, while this cancellation results in the perfect-looking of the derivative of the Lyapunov function, and it does not necessarily mean that good performance is ensured. To overcome these problems, another controller was proposed in the last 10 years, and it is used in several areas for the control applications. This controller is known as the active disturbance rejection controller (ADRC), and it is proposed by Han in 2009 [17].

The prospective of ADRC as an effective new control strategy is evident in many case studies, where the technique is used to address a number of benchmark problems in diverse industry sectors, with promising results. However, to the author's best knowledge, very few publications are available in the literature documenting the issue of controlling the hybrid PV-wind energy conversion systems but in a separate way. In [18], the authors have proposed a predictive ADRC to overcome the time delay in PMSG wind turbine systems, and in [19], control of active and reactive powers in a DFIG-based WECS by the ADRC technique has been discussed, and in [20], the author proposed an active disturbance rejection control to a solar PV DC-DC converter. The main advantages of this controller lies on the real-time rejection of internal and external disturbances based on an extended state observer (ESO) [21]. The variation of internal parameters or modeling errors as internal disturbances and the instability of the grid as external disturbances are caused either by voltage dips and frequency droops. As a result, this paper presents the application of a new linear ADRC to the hybrid PV-wind energy conversion system.

Our main contribution in this work lies on the development of a new robust control strategy for the grid-connected hybrid PV-wind energy conversion system by ADRC, in order to extract the maximum power available from the PV-wind system and to control the power delivery. The voltage based perturb and observe technique is used to extract the maximum power from the PV system, while the optimal torque control technique is used for the WECS. The linear ADRC is utilized to regulate the DC bus voltage and to ensure the control of active and reactive powers. For this purpose, this paper is structured as follows: Section 2 presents the overall architecture of the proposed system and its modeling components. Section 3 introduces the mathematical model of the active disturbance rejection controller. Section 4 gives the proposed control by ADRC for the hybrid system, while in Section 5, the simulation results of the wind energy conversion system are presented.

2. Mathematical Modeling and Architecture of the Proposed System

The proposed system as demonstrated in Figure 1 consists of a variable speed direct-driven wind turbine based on permanent magnetic synchronous generator (PMSG), a photovoltaic array, a DC/DC converter, an AC/DC converter, a common DC bus capacitor, and a grid interface inverter with an RL filter. The PV generator is controlled by the boost converter to track the maximum power point by using the MPPT technique. The WEC system which involves a wind turbine directly connected to the PMSG and is controlled by the AC/DC converter to extract the maximum power from the wind. These two energy sources are connected in parallel with a common DC link through their individual converters, where a voltage source inverter (VSI) is utilized to supply the total generated power into the grid while ensuring a unit power factor.

2.1. Mathematical Equivalent Model of PV Array. In order to set up the PV model, it is necessary to establish its equivalent electrical circuit. Indeed, the literature cites numerous mathematical models [22] representing the very strong nonlinear behavior of the PV model due to their design based on semiconductor junctions. These models differ from each other depending on the number of parameters involved in calculating the voltage and current delivered by the PV module. The single- and the double-diode models are generally used to model the solar cell behavior. The double-diode model is adopted in this paper [22], and its equivalent circuit is given in Figure 2. It consists of two diodes (D_1, D_2) characterizing the P-N junction, a current source (I_{ph}) characterizing the photocurrent, a series resistor (R_s) representing the losses by the Joule effect, and a shunt resistor (R_{sh}) characterizing the leakage current.

The cell model can then be expressed by

$$\begin{aligned} I_{cell} &= I_{ph} - I_{d1} - I_{d2} - I_{sh}, \\ I_{d1} &= I_{sc1} \left(\exp \left[\frac{(V_{cell} + R_s \cdot I_{cell})}{a_1 \cdot V_{th}} \right] - 1 \right), \\ I_{d2} &= I_{sc2} \left(\exp \left[\frac{(V_{cell} + R_s \cdot I_{cell})}{a_2 \cdot V_{th}} \right] - 1 \right), \\ I_{sh} &= \frac{V_{cell} + R_s \cdot I_{cell}}{R_{sh}}, \end{aligned} \quad (1)$$

where I_{sc1} and I_{sc2} are the reverse saturation current of the diodes, a_1 and a_2 are the ideality factors of diodes, and V_{th} is the cell thermal voltage, $V_{th} = k \cdot (T/q)$, where T is the junction P-N temperature, k is Boltzmann's constant (1.38×10^{-23} (J/K)), and q is the electron charge (1.602×10^{-19} C).

2.2. Wind Turbine Modeling. In any wind energy conversion system, the purpose of the turbine is to harness the wind kinetic energy and transform it into mechanical energy that rotates an electric generator. The modeling of a wind turbine consists in expressing the extracted aerodynamic power P_{aero} as a function of the incident wind speed V , and its expression is given by

$$P_{aero} = C_p(\lambda, \beta) P_W = C_p(\lambda, \beta) \frac{\rho s v^3}{2}. \quad (2)$$

Its aerodynamic torque T_{aero} is given by the following expression:

$$T_{aero} = \frac{1}{2\Omega_t} C_p(\lambda, \beta) \rho s v^3, \quad (3)$$

where ρ is the air density, generally taken equal to 1.225 kg/m^3 .

The wind turbine aerodynamic efficiency is represented by a power factor called C_p [23]. This coefficient depends on the turbine characteristics (speed ratio λ and pitch angle β). Figure 3 represents the C_p characteristics:

$$C_p(\lambda, \beta) = -0.6175 \left(\frac{116}{\lambda} - 0.4\beta - 5 \right) e^{-21/\lambda} + 0.1405\lambda, \quad (4)$$

$$\lambda = \frac{\Omega_t R}{V}, \quad (5)$$

$$\frac{1}{\lambda'} = \frac{1}{\lambda + 0.08\beta} - \frac{0.035}{\beta^3 + 1}, \quad (6)$$

where Ω_t is the turbine rotational speed. The mechanical equation of the turbine shaft which is rigidly connected to the synchronous generator is given by [24]

$$J \frac{d\Omega_t}{dt} = T_{aero} - T_{em} - f\Omega_t, \quad (7)$$

where J is the system total inertia, f is the friction coefficient, and T_{em} represents the generator electromagnetic torque.

2.3. Permanent Magnet Synchronous Generator Modeling. Generally, to represent a state model, we define the state vector x , the input vector u , and the output vector y . This model is written in the following form:

$$\begin{aligned} \dot{x} &= Ax + Bu, \\ y &= Hx. \end{aligned} \quad (8)$$

For the PMSG, the input vector is composed of the stator voltages. The state vector consists of electrical quantities (currents) and mechanical quantities (speed and position). The nonlinear state model in the d-q frame is described by the system below:

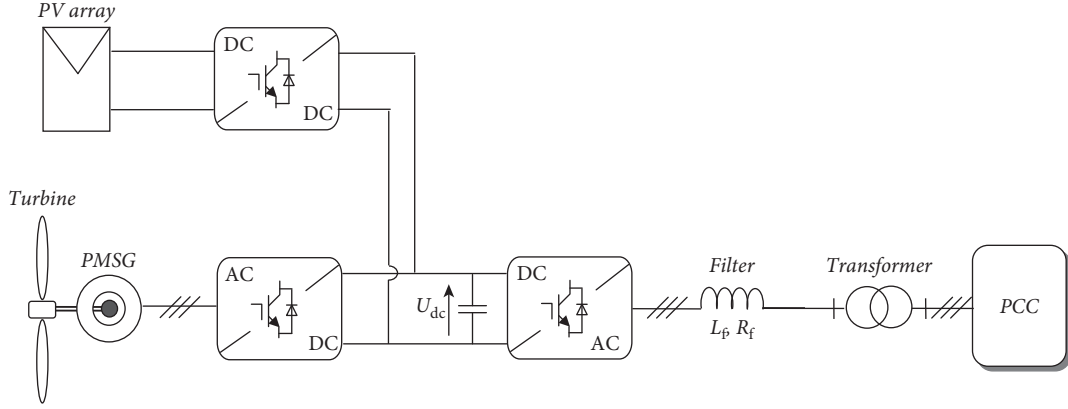


FIGURE 1: Grid-connected variable speed wind energy conversion system based on the permanent magnet synchronous generator.

$$\begin{pmatrix} \dot{i}_d \\ \dot{i}_q \\ \dot{\omega} \\ \dot{\theta} \end{pmatrix} = \begin{pmatrix} \frac{-R_s}{L_d} & \frac{\omega L_q}{L_d} & 0 & 0 \\ \frac{-\omega L_d}{L_q} & \frac{-R_s}{L_q} & \frac{\psi_f}{L_q} & 0 \\ 0 & 0 & 0 & 0 \\ 0 & 0 & 1 & 0 \end{pmatrix} \begin{pmatrix} i_d \\ i_q \\ \omega \\ \theta \end{pmatrix}$$

$$+ \begin{pmatrix} \frac{-1}{L_d} & 0 \\ 0 & \frac{-1}{L_q} \\ 0 & 0 \\ 0 & 0 \end{pmatrix} \begin{pmatrix} v_d \\ v_q \\ 0 \\ 0 \end{pmatrix} \quad (9)$$

$$\text{or } x = [i_d i_q \omega \theta]^T,$$

$$u = [v_d v_q]^T,$$

$$y = [i_d i_q]^T,$$

$$H = \begin{pmatrix} 1 & 0 & 0 & 0 \\ 0 & 1 & 0 & 0 \end{pmatrix},$$

where R_s represents the stator resistance, L_d and L_q are the direct and quadrature inductances, i_d and i_q are the stator currents in the d-q frame, ψ_f is the permanent magnet flux, ω is the PMSG speed, and it is given by $\omega = P\Omega_r$, and P are the pair poles [25].

The electromagnetic torque is given by

$$T_{em} = \frac{3}{2}P[(L_d - L_q)i_d i_q + i_q \psi_f]. \quad (10)$$

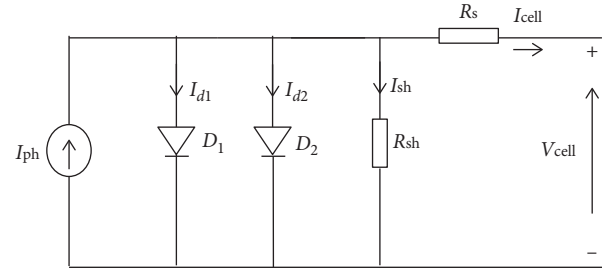


FIGURE 2: Double-diode PV cell models.

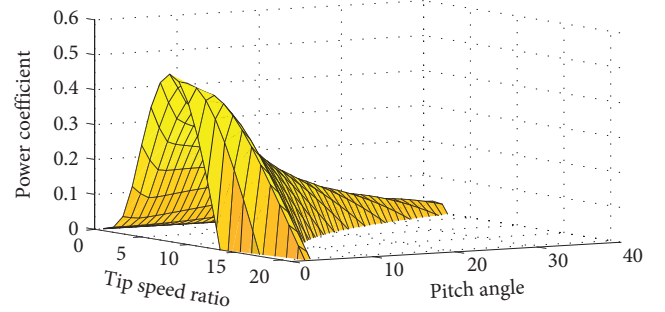


FIGURE 3: Power coefficient characteristics for various values of pitch angle β and tip speed ratio λ .

2.4. DC Link and Filter Modeling. The interconnection between the hybrid energy conversion system and the utility power grid is carried out via an RL filter (L_f , R_f) as illustrated in Figure 4. This filter is used to prevent harmonic currents from spreading through the grid [26]:

$$\begin{cases} V_{s-a} = V_{fa} - R_f i_{fa} - L_f \frac{di_{fa}}{dt}, \\ V_{s-b} = V_{fb} - R_f i_{fb} - L_f \frac{di_{fb}}{dt}, \\ V_{s-c} = V_{fc} - R_f i_{fc} - L_f \frac{di_{fc}}{dt}. \end{cases} \quad (11)$$

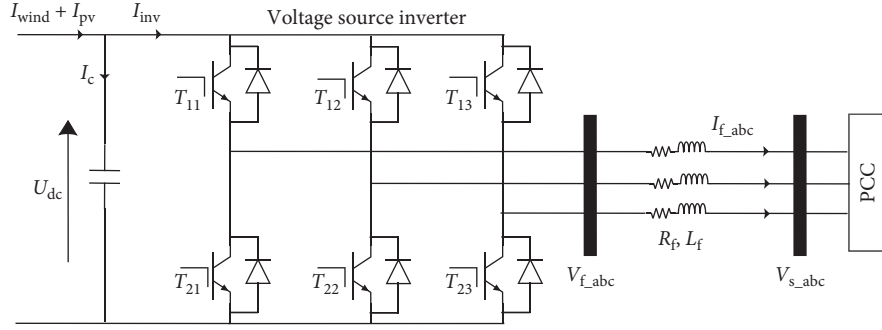


FIGURE 4: The connection of the hybrid energy conversion system with the utility grid.

Applying Park's transformation, equation (11) becomes in d-q frame as follows:

$$\begin{cases} V_{gd} = V_{fd} - R_f i_{fd} - L_f \frac{di_{fd}}{dt} + L_f \omega_g i_{fq}, \\ V_{gq} = V_{fq} - R_f i_{fq} - L_f \frac{di_{fq}}{dt} - L_f \omega_g i_{fd}, \end{cases} \quad (12)$$

where v_{fd} and v_{fq} are the inverter voltage components, v_{gd} and v_{gq} are the grid voltages, and i_{fd} and i_{fq} are the filter currents.

The modeling of the DC-link bus is given by

$$\frac{dU_{dc}}{dt} = \frac{1}{C} (i_{wind} + i_{pv} - i_{inv}), \quad (13)$$

where C is the DC-link capacitor.

3. Proposed Control Strategy for the HRES by ADRC

The proposed control scheme for the grid-connected hybrid energy conversion system is given as follows:

- (i) VPO-MPPT based on ADRC is used to enhance the photovoltaic energy conversion system (PVECS) efficiency under irradiation changes
- (ii) OTC-MPPT based on ADRC is used to enhance the WECS efficiency under wind velocity changes
- (iii) VOC based on ADRC is used to control the DC-link voltage and to regulate the injection of the produced active and reactive powers into the grid

3.1. Mathematical Model of ADRC. Active disturbance rejection control (ADRC) is a robust control strategy proposed by Han [17]. The principal concept of this method is to treat the internal and external uncertainties as a "generalized disturbances," try to estimate them in real time by using an extended state observer (ESO), and then use it in the feedback control law with the objective to compensate the disturbances rapidly. A first-order ADRC configuration is shown in Figure 5. It mainly consists of three parts: tracking differentiator (TD), extended state observer (ESO), and nonlinear state error feedback (NLSEF).

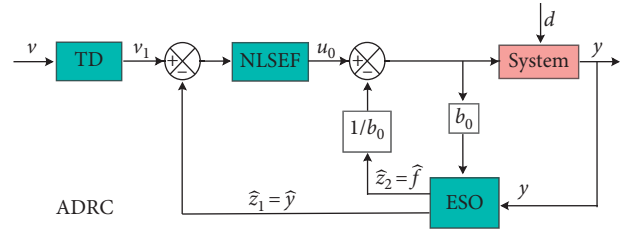


FIGURE 5: Block diagram of a first-order active disturbance rejection controller.

In Figure 5, v is the input signal, v_1 is the input tracking signal, y is the system feedback signal, z_1 is the estimated tracking signal, z_2 is the total disturbance estimation, b_0 is the compensation factor, z_2/b_0 is the internal and external disturbance compensation, u_0 is the initial control object by NLSEF, and u is the final control signal after disturbance compensation.

For a first-order controlled object, its mathematical model of ADRC is set as [27]

$$\begin{cases} \varepsilon_0 = v_1 - v, \\ \frac{dv_1}{dt} = -r \text{fal}(\varepsilon_0, \alpha_0, \delta_0), \end{cases} \quad (14)$$

$$\begin{cases} \varepsilon = z_1 - y, \\ \frac{dz_1}{dt} = z_1 - \beta_0 \text{fal}(\varepsilon, \alpha, \delta) + bu(t), \\ \frac{dz_2}{dt} = \beta_0 \text{fal}(\varepsilon, \alpha, \delta), \end{cases} \quad (15)$$

$$\begin{cases} \varepsilon_1 = v_1 - z_1, \\ u_0 = \beta_1 \text{fal}(\varepsilon_1, \alpha_1, \delta_1), \\ u = u_0 - \frac{z_2}{b_0}, \end{cases} \quad (16)$$

$$\text{fal}(\varepsilon, \alpha, \delta) = \begin{cases} |\varepsilon|^\alpha \text{sgn}(\varepsilon), & |\varepsilon| > \delta, \\ \frac{\varepsilon}{\delta^{1-\alpha}}, & |\varepsilon| \leq \delta, \end{cases} \quad (17)$$

where the mathematical model of the TD is defined by using equation (14), the model of ESO is given by equation (15), and for NLSEF block, it is represented by equation (16). β_{01} , β_{02} , and β_1 are the output error factors, $\text{fal}(\varepsilon, \alpha, \delta)$ is the best function which is defined by using equation (17), δ is the filtering factor to ESO, and α is a nonlinear factor.

In practice, the ADRC needs to adjust a large number of parameters, and adjusting these parameters is complicated. So as to reduce the model complexity and the controller computational, a linear ADRC design method is proposed and applied to the hybrid PV-wind energy conversion system.

3.2. Linear ADRC Design. To illustrate the principle of ADRC [28], a nonlinear and time-varying dynamic system of n order is considered, with only a single input $u(t)$ and an output, and it can be described by the following equation:

$$y^{(n)}(t) = f(y(t), y^{(1)}(t), y^{(2)}(t), \dots, y^{(n-1)}(t), u(t)) + d(t) + b_0 \cdot u(t), \quad (18)$$

where $f(y(t), y^{(1)}(t), y^{(2)}(t), \dots, y^{(n-1)}(t), u(t))$ represents the model internal dynamics which is assumed to be unknown, $d(t)$ represents the external disturbances, and b_0 represents the known system parameter.

The following terms $f(t) = f(y(t), y^{(1)}(t), y^{(2)}(t), \dots, y^{(n-1)}(t), u(t)) + d(t)$ are considered as all the internal and external disturbances affecting the system to be controlled.

Therefore, the system equation is rewritten in the following form:

$$y^{(n)}(t) = f(t) + b_0 \cdot u(t). \quad (19)$$

Instead of looking for an explicit mathematical model of $f(t)$, ADRC offers another alternative that significantly reduces the dependence of the control on accurate system modeling, as the proposed strategy consists in estimating $f(t)$, and then to cancel it in real time using an appropriate control signal $u(t)$. To do so, an extended state observer is used. Let

$$\begin{aligned} z_1 &= y, \\ z_1 &= \dot{y}, \dots, z_n = y^{(n-1)}, \\ z_{n+1} &= f. \end{aligned} \quad (20)$$

Assume that f is differentiable and let $\dot{f} = h$. Then equation (19) can be written as

$$\begin{cases} \dot{z} = Az + Bu + Eh, \\ y = Cz, \end{cases} \quad (21)$$

where

$$z = [z_1, z_2, \dots, z_n, z_{n+1}]^T, \\ A_{(n+1, n+1)} = \begin{bmatrix} 0 & 1 & 0 & \dots & 0 \\ 0 & 0 & 1 & \dots & 0 \\ \vdots & \vdots & \vdots & \ddots & \vdots \\ 0 & 0 & 0 & \dots & 1 \\ 0 & 0 & 0 & \dots & 0 \end{bmatrix},$$

$$\begin{aligned} B_{(n+1, 1)} &= [1 \ 0 \ \dots \ 0 \ 0]^T, \\ E_{(n+1, 1)} &= [0 \ 0 \ \dots \ 0 \ 1]^T, \\ B_{(1, n+1)} &= [1 \ 0 \ \dots \ 0 \ 0]^T. \end{aligned} \quad (22)$$

A full-order Luenberger state observer can be designed as

$$\begin{cases} \dot{\hat{z}}(t) = A\hat{z} + Bu + L(y - \hat{y}), \\ \hat{y} = C\hat{z}, \end{cases} \quad (23)$$

where L is the observer gain vector.

The error between the actual value z and the estimated value \hat{z} by the observer can be written in the following form:

$$e(t) = z - \hat{z}. \quad (24)$$

The dynamics of the estimation error is therefore expressed by

$$\dot{e} = (A - LC)e, \quad (25)$$

where

$$A - LC = \begin{bmatrix} -\beta_1 & 1 & 0 & \dots & 0 \\ -\beta_2 & 0 & 1 & \dots & 0 \\ \vdots & \vdots & \vdots & \ddots & \vdots \\ -\beta_n & 0 & 0 & \dots & 1 \\ -\beta_{n+1} & 0 & 0 & \dots & 0 \end{bmatrix}. \quad (26)$$

In order to ensure asymptotic convergence of the estimation error ($e \rightarrow 0$ when $t \rightarrow \infty$) and therefore a good functioning of the observer, it is necessary that the parameters of the gain matrix L are chosen in such a way that $(A - LC)$ forms a Hurwitz matrix; that is to say, the poles of its polynomial characteristic $P_{\text{ESO}}(s)$ are all with strictly negative real parts:

$$\begin{aligned} P_{\text{ESO}}(s) &= \det(sI_{n+1} - (A - LC)) = s^{n+1} + \beta_1 s^n + \beta_2 s^{n-1} \\ &+ \dots + \beta_n s + \beta_{n+1}. \end{aligned} \quad (27)$$

The observer's gains are generally determined by the pole placement technique. A compromise must be established between the speed at which the observer follows the states and his sensitivity to noise measurement. The faster the ESO is, the earlier the disturbance is estimated and cancelled by the corrector. This is achieved by placing the observer's poles well to the left of the observed system poles the P -plan. This choice leads to the adoption of a large bandwidth for the extended state observer. However, it should be remembered that too much bandwidth can harm the system by promoting noise transmission [28].

Taking into account all these constraints, the cutoff pulse of the extended state observer ω_o is chosen to have a suitable stabilization time, and its $(n + 1)$ poles are placed to $-\omega_o$:

$$P_{\text{ESO}}(s) = s^{n+1} + \beta_1 s^n + \beta_2 s^{n-1} + \dots + \beta_n s + \beta_{n+1} = (s + \omega_o)^{n+1}. \quad (28)$$

The observer's gains are then expressed as follows:

$$\beta_i = \frac{(n+1)!}{(n+1-i)!} \omega_o^i. \quad (29)$$

Therefore, when $(A-LC)$ is asymptotically stable, $\hat{z}_1, \hat{z}_2, \dots, \hat{z}_n$ will approximate y and its derivatives (up to order $n-1$), and \hat{z}_{n+1} will approximate the generalized disturbance f . Consequently, the estimated generalized disturbances can be applied in control to reject it more quickly.

If the control law is chosen as

$$u(t) = \frac{u_0(t) - \hat{z}_{n+1}(t)}{b_0}, \quad (30)$$

then the system equation (19) becomes

$$y^{(n)}(t) = f(t) - \hat{z}_{n+1}(t) + u_0(t). \quad (31)$$

If \hat{z}_{n+1} is a correct estimation of f ($\hat{z}_{n+1} \approx f$), then the system is reduced to an n -order integral system:

$$y^{(n)}(t) = u_0(t). \quad (32)$$

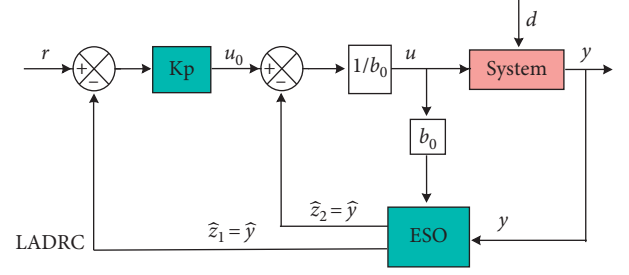


FIGURE 6: Block diagram of a first-order linear ADRC.

Therefore, the final system can be controlled by the corresponding state-feedback control law:

$$u_0(t) = k_1(r(t) - y(t)) + k_2(\dot{r}(t) - \dot{y}(t)) + \dots + k_n(r^{(n-1)}(t) - y^{(n-1)}(t)), \quad (33)$$

where $r(t)$ is the reference signal.

Since $\hat{z}_1(t), \dots, \hat{z}_n(t)$ is a correct estimation of $y(t), \dots, y^{(n-1)}(t)$, then the final control law can be approached as

$$u(t) = \frac{k_1(r(t) - \hat{z}_1(t)) + \dots + k_n(r^{(n-1)}(t) - \hat{z}_n(t)) - \hat{z}_{n+1}(t)}{b_0} = K_0(\hat{r}(t) - \hat{z}(t)), \quad (34)$$

where

$$\hat{r}(t) = [r(t)\dot{r}(t), \dots, r^{(n-1)}(t)0]^T, \quad (35)$$

$$K_0 = \frac{[k_1, k_2, \dots, k_n 1]}{b_0}. \quad (36)$$

The linear active disturbance rejection controller can be summarized and designed by

$$\begin{cases} \dot{\hat{z}}(t) = A\hat{z}(t) + Bu(t) + L[y(t) - C\hat{z}(t)] \\ \quad = (A-LC)\hat{z}(t) + Bu(t) + Ly(t), \\ u(t) = K_0[\hat{r}(t) - \hat{z}(t)]. \end{cases} \quad (37)$$

The structure of the first-order LADRC is depicted in Figure 6.

4. Control of the Machine-Side Converter by ADRC

The control of the machine-side converter is obtained by using the linear ADRC, and it regulates the stator currents with its references, where Is_{d-ref} is set to zero and Is_{q-ref} is given by the optimal torque control OTC-MPPT [29] block as depicted in Figure 7.

4.1. MPPT Analysis for the Variable Speed Wind Turbine. To ensure maximum power extraction from the wind turbine, the rotational speed must be maintained at the

optimum value of the tip speed ratio λ_{opt} which makes the turbine operating at $C_p = C_{p,max}$.

Considering the relationship between the wind speed V and the tip speed ratio λ in equation (5), the wind turbine power can be expressed as a function of the rotational speed Ω_m :

$$P_t = 0.5\rho\pi R^5 \frac{C_p(\lambda, \beta)}{\lambda^3} \omega_m^3. \quad (38)$$

Replacing λ by λ_{opt} and placing in $C_p(\lambda, \beta) = C_{p,max}$, the wind turbine maximum power can be expressed as

$$P_{t,max} = K_{opt}\omega_m^3, \quad (39)$$

where K_{opt} is a coefficient given by

$$K_{opt} = 0.5\rho\pi R^5 \frac{C_{p,max}}{\lambda_{opt}^3}. \quad (40)$$

So the torque reference T_{em-ref} is expressed as follows:

$$T_{em-ref} = K_{opt}\omega_m^2. \quad (41)$$

4.2. Linear ADRC Design for Machine-Side Converter. The zero direct axis control (ZDC) is used to obtain the references of currents used in control [29]. The three-phase stator currents $i_{s,abc}$ are converted into $d-q$ axis frame using Park's transformation technique, and then, the d -axis current a is

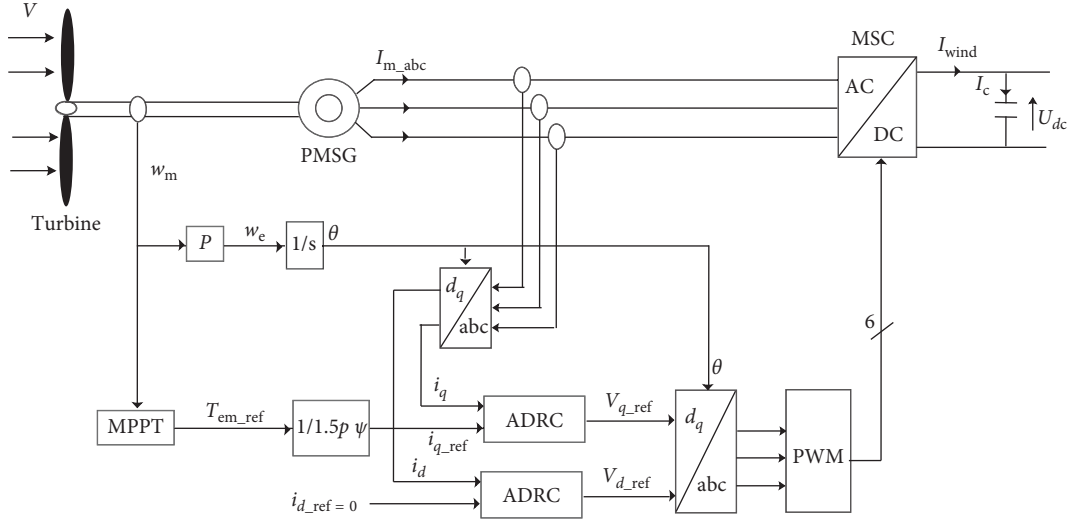


FIGURE 7: Machine-side converter control by ADRC.

set to be zero and the q -axis current i_q is set to be equal to the stator current i_s :

$$i_s = \sqrt{i_d^2 + i_q^2} = i_q. \quad (42)$$

Consequently, for $i_d = 0$, the electromagnetic torque can be controlled by i_q :

$$T_{em} = \frac{3}{2} P \psi_f i_q. \quad (43)$$

Hence,

$$\begin{aligned} T_{em-ref} &= \frac{3}{2} P \psi_f i_{q-ref}, \\ i_{q-ref} &= \frac{2}{3 P \psi_f} T_{em-ref}. \end{aligned} \quad (44)$$

The stator current regulations are achieved by two ADRC, where the equations of i_d and i_q are adapted to the canonical form of ADRC:

$$\frac{dy(t)}{dt} = f(y, d, t) + b_0 u(t). \quad (45)$$

For the d -axis current, we have

$$\frac{di_d(t)}{dt} = -\frac{R_s}{L_d} i_d + \omega_e i_q \frac{L_q}{L_d} + \frac{v_d}{L_d}, \quad (46)$$

where

$$\begin{cases} f(y, d, t) = -\frac{R_s}{L_d} i_d + \omega_e i_q \frac{L_q}{L_d}, \\ b_0 = \frac{1}{L_d}, \\ u = v_d, \end{cases} \quad (47)$$

and for the q -axis, we have

$$\frac{di_q(t)}{dt} = -\frac{R_s}{L_q} i_q - \omega_e i_d \frac{L_d}{L_q} - \frac{\psi_f}{L_q} + \frac{v_q}{L_q}, \quad (48)$$

$$\begin{cases} f(y, d, t) = -\frac{R_s}{L_q} i_q - \omega_e i_d \frac{L_d}{L_q} - \frac{\psi_f}{L_q}, \\ b_0 = \frac{1}{L_q}, \\ u = v_q. \end{cases} \quad (49)$$

5. Control of the DC-DC Converter by ADRC

To obtain the optimal exploitation of the PVECS during the change of environmental conditions, a two-stage control strategy is proposed and adopted here [30]. As illustrated in Figure 8, firstly, a PO-based voltage MPPT is used to generate the reference voltage V_{mpp} . After that, an improved cascaded loop based on linear ADRC is used to track the PV voltage and current in order to extract the maximum power from the PV array.

5.1. P and O-Based V-MPPT. The main aim of the VO-MPPT is to generate the reference voltage V_{mpp} corresponding to the maximum power point. For this purpose, P and O-based V-MPPT [30] technique is utilized due to its featuring effectiveness and simplicity as shown in Figure 9.

5.2. ADRC Design for the V-MPPT. Because of the almost zero variation in PV voltage at the MPP under irradiation changes, V-MPPT is considered as an effectiveness alternative. However, the efficiency of this method depends on the cascaded V/I control loop concept. In this section, a robust cascaded V/I control loop based on ADRC is proposed and demonstrated to track the MPP under weather changes.

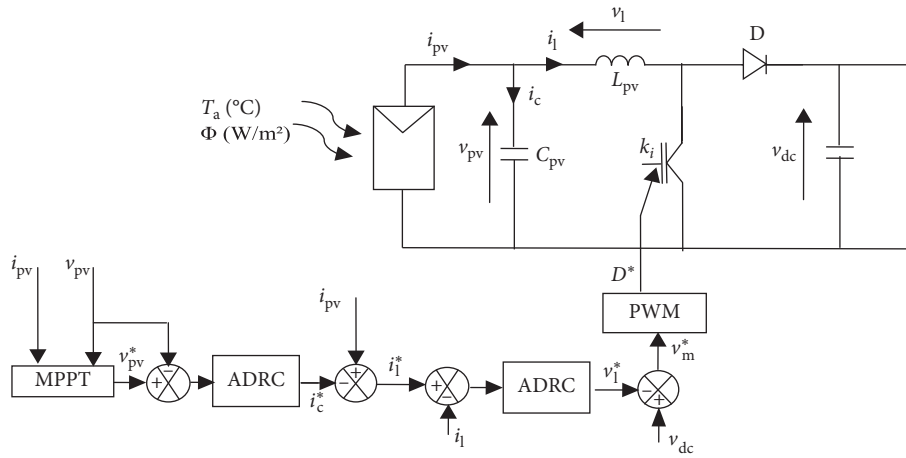


FIGURE 8: Control of the DC-DC converter linear ADRC.

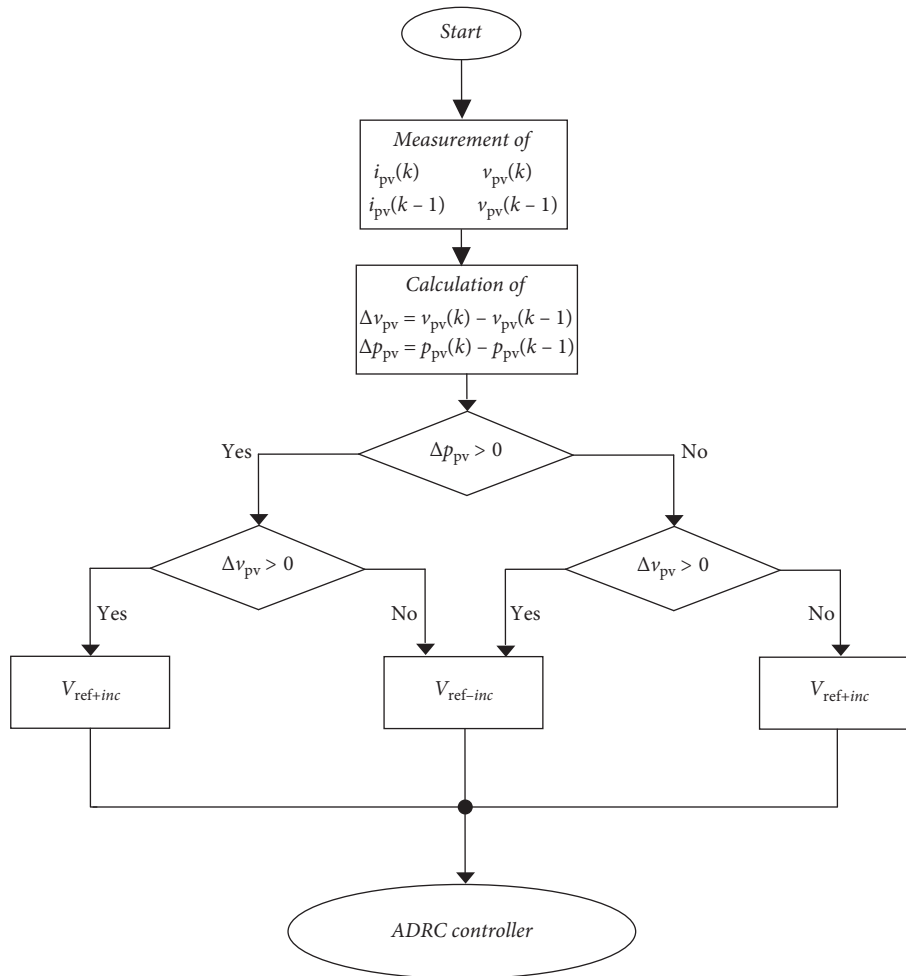


FIGURE 9: P and O-based V-MPPT.

The outer loop of the proposed strategy consists in controlling the V_{pv} voltage to its reference obtained by the V-MPPT. The dynamic of the V_{pv} voltage is expressed as follows:

$$\frac{dV_{pv}}{dt} = \frac{1}{C_{pv}} i_c \tag{50}$$

Then, the ADRC for the outer loop can be designed as follows:

$$\begin{cases} f(y, d, t) = \Delta C_{pv}, \\ b_0 = \frac{1}{C_{pv}}, \\ u = i_c. \end{cases} \quad (51)$$

For the inner loop, it is used to regulate the current across the inductor. Its dynamics is presented below:

$$\frac{di_1}{dt} = \frac{1}{L}v_1. \quad (52)$$

Then, the ADRC for the inner loop can be designed as follows:

$$\begin{cases} f(y, d, t) = \Delta L, \\ b_0 = \frac{1}{L}, \\ u = v_1. \end{cases} \quad (53)$$

6. Control of the Grid-Side Converter by ADRC

The grid-side control consists of two cascade control loops in which its main purpose is to stabilize the DC-link voltage and to control the active and reactive powers injected to the grid during variation in environmental conditions. The inner loop will control the filter currents, and the outer loop will control the DC bus voltage. The inner loop dynamics is settled to be faster than the outer one. The GSC can be controlled either by voltage-oriented control (VOC) or direct power control (DPC) technique. VOC is considered to be more efficient due to lower energy losses and to lower current distortion compared to DPC [31].

As illustrated in Figure 10, VOC is used to control the GSC and it involves a dual-loop control structure: an outer loop to control the DC-link voltage and an inner loop to control the grid currents.

The phase-locked loop (PLL) device is used to obtain the phase angle and frequency from the grid voltages [32]. The d -axis component of the synchronous reference frame is aligned with the grid voltage $v_{dg} = v_g$ and the q -axis component was set to zero $v_{qg} = 0$.

The active and reactive powers are then given by

$$\begin{cases} P_g = \frac{3}{2}v_{gd}i_{fd}, \\ Q_g = -\frac{3}{2}v_{gd}i_{fq}. \end{cases} \quad (54)$$

This shows that the active and reactive powers will be controlled, respectively, by currents i_{fd} and i_{fq} .

6.1. DC Bus Voltage Control by LADRC. The power across the DC-link capacitor C can be expressed by

$$P_{dc} = U_{dc}(i_{wind} + i_{pv} - i_{inv}). \quad (55)$$

By substituting equation (13) with equation (55), we get

$$P_{dc} = CU_{dc} \frac{dU_{dc}}{dt}. \quad (56)$$

If all the losses in the filter, the power electronics converters, and in the capacitor are neglected, the exchanged powers on the DC bus are expressed by

$$P_{dc} = P_s + P_{pv} - P_g, \quad (57)$$

where P_s , P_{pv} , and P_g are the generator, PV system, and grid powers, respectively.

By taking into account equations (54)–(56), the DC bus voltage can be expressed by

$$CU_{dc} \frac{dU_{dc}}{dt} = U_{dc}(i_{wind} + i_{pv}) - \frac{3}{2}v_{gd}i_{fd}, \quad (58)$$

$$\text{or } \frac{dU_{dc}^2}{dt} = \frac{2U_{dc}}{C}(i_{wind} + i_{pv}) - \frac{3v_{gd}}{C}i_{fd}, \quad (59)$$

and we put $X = U_{dc}^2$:

$$\frac{dX}{dt} = \frac{2\sqrt{X}}{C}(i_{wind} + i_{pv}) - \frac{3v_{gd}}{C}i_{fd}, \quad (60)$$

so we obtain

$$\begin{cases} f(y, d, t) = \frac{2\sqrt{X}}{C}(i_{wind} + i_{pv}), \\ b_0 = -\frac{3v_{gd}}{C}, \\ u = i_{fd}. \end{cases} \quad (61)$$

6.2. Control of Filter Currents by LADRC. The external voltage regulation loop makes it possible to maintain the voltage across the capacitor U_{dc} and to generate the current reference i_{fd-ref} for the internal current loop.

For the current i_{fq-ref} , it is calculated by the desired delivery of reactive power:

$$i_{fq-ref} = -\frac{2}{3v_{gd}}Q_{f-ref}. \quad (62)$$

Then, similarly to the machine-side control, the filter currents are given in canonical form of ADRC.

For d -axis current,

$$\frac{di_{fd}}{dt} = \frac{1}{L_f}(-R_f i_{fd} - v_{gd} + L_f \omega_g i_{fq}) + \frac{v_{fd}}{L_f}, \quad (63)$$

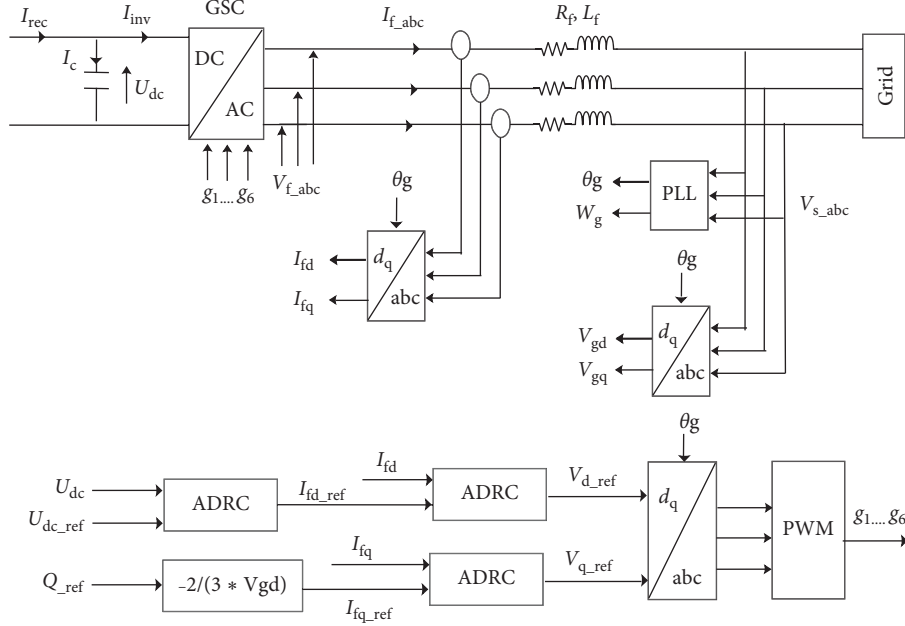


FIGURE 10: Grid-side converter control by linear ADRC.

where

$$\begin{cases} f(y, d, t) = \frac{1}{L_f} (-R_f i_{fd} - v_{gd} + L_f \omega_g i_{fq}), \\ b_0 = \frac{1}{L_f}, \\ u = v_{fd}. \end{cases} \quad (64)$$

For q -axis current,

$$\frac{di_{fq}}{dt} = \frac{1}{L_f} (-R_f i_{fq} - L_f \omega_g i_{fd}) + \frac{v_{fq}}{L_f}, \quad (65)$$

where

$$\begin{cases} f(y, d, t) = \frac{1}{L_f} (-R_f i_{fq} - L_f \omega_g i_{fd}), \\ b_0 = \frac{1}{L_f}, \\ u = v_{fq}. \end{cases} \quad (66)$$

7. Results and Discussion

7.1. Simulation Results. To validate the theoretical study and the effectiveness of the presented control strategy, a complete structure of HRES is designed and simulated under MATLAB/Simulink environment. The simulation parameters are given in appendix.

The applied wind speed profile is shown in Figure 11. Figures 11–18 present the simulations results of the proposed strategy for the WECS system.

As can be noticed in Figures 12 and 13, the mechanical speed and the extracted power take the same form as the wind profile, and it is also shown in Figure 14 that the power coefficient has been maintained at its optimal value ($C_{p\max} = 0.43$) which shows the effectiveness of the MPPT strategy in terms of maximum power extraction.

The response of the ADRC shows good tracking characteristics as highlighted in Figures 15 and 16 where the direct axis current I_d was maintained to be zero and the quadrature current I_q tracks its references. The generated active power and stator currents are shown in Figures 17 and 18.

For the PVECS, the applied profile of the irradiation is illustrated in Figure 19 and the corresponding results are demonstrated in Figures 20–22.

As can be noticed in Figures 20 and 21, the V_{pv} voltage is regulated with its references that is obtained from the VPO-MPPT and the inductor current is also regulated to its references, which ensures the extraction of the maximum PV power as illustrated in Figure 22.

Figure 23 shows that the DC-link voltage V_{dc} is maintained at its reference with some fluctuations which are due to the stochastic nature of wind speed. Also we notice in Figures 24 and 25 that the linear ADRC regulates the grid currents to their references.

The control of the active and reactive powers is also achieved as shown in Figures 26–28 where the extracted power from the HECS was injected into the grid and the reactive power was set to zero to ensure a unit power factor.

In order to test the robustness of the proposed control strategy, another test was carried out in which we have changed the internal parameters of the PMSG, the stator resistance, and inductance L_s , by an increase of 50% of their nominal value. The results obtained by LADRC are compared with the classical PI controller. The utilized wind

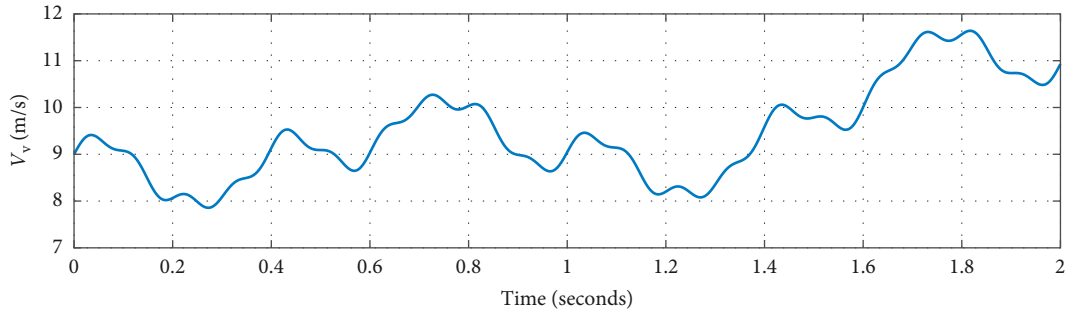


FIGURE 11: Wind speed profile.

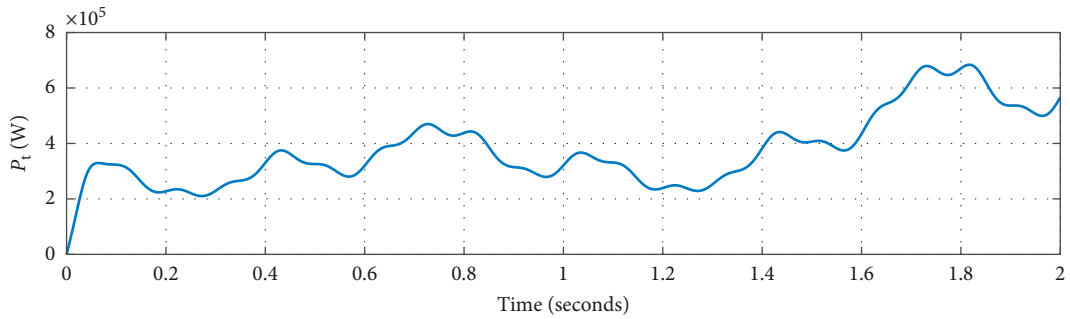


FIGURE 12: Turbine mechanical power.

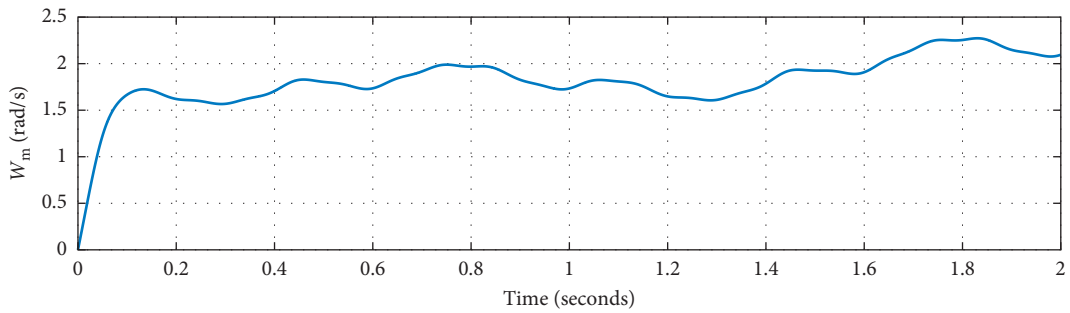


FIGURE 13: PMSG speed in rad/s.

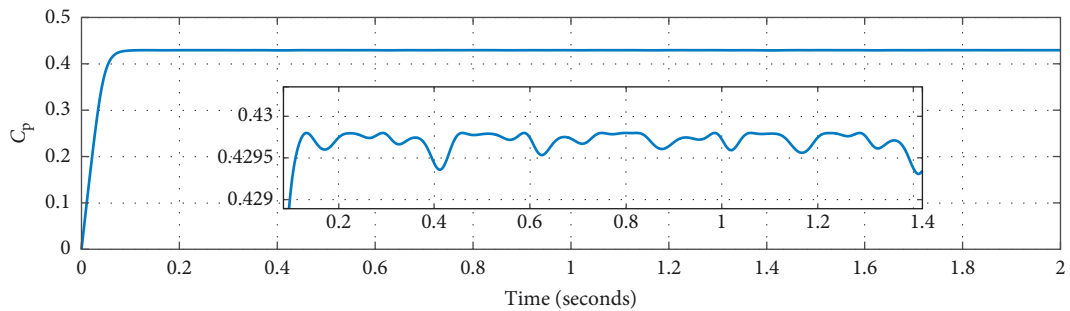


FIGURE 14: Power coefficient C_p .

speed profile is given in Figure 29. For the PV system, the irradiation was maintained at 1000 W/m^2 .

As shown in Figure 30, both controllers regulate the current I_d to zero, but the ADRC has a faster response compared to the PI controller.

It can be noticed in Figure 31 that the current I_q was regulated to its reference and that the response of LADRC is better than the PI one. So as a closing statement, the simulation results have demonstrated that the proposed strategy is efficient in terms of stability, rapidity, accuracy, and

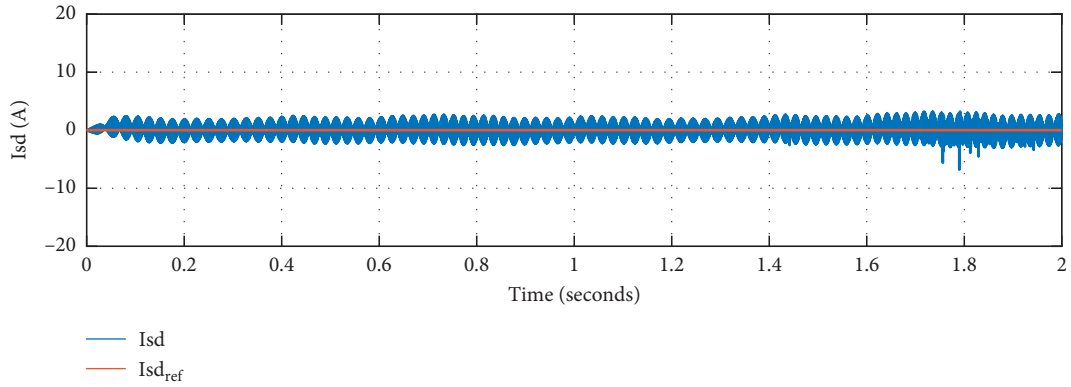


FIGURE 15: Stator d -axis current I_d .

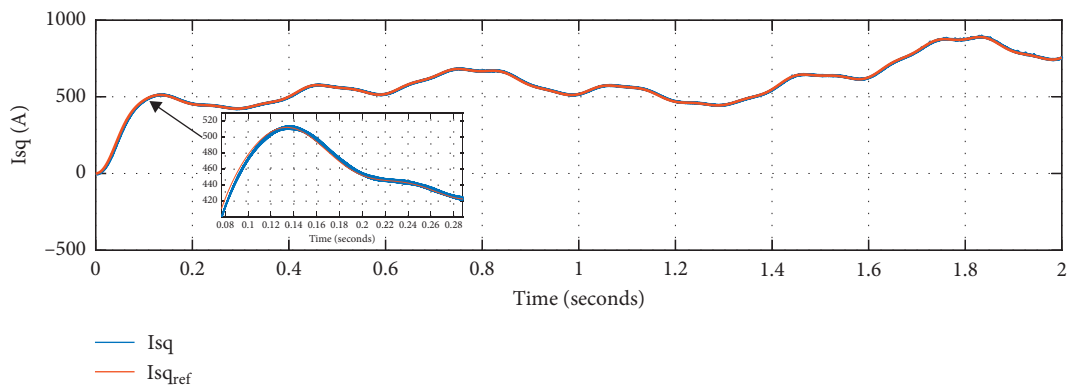


FIGURE 16: Stator q -axis current I_q .

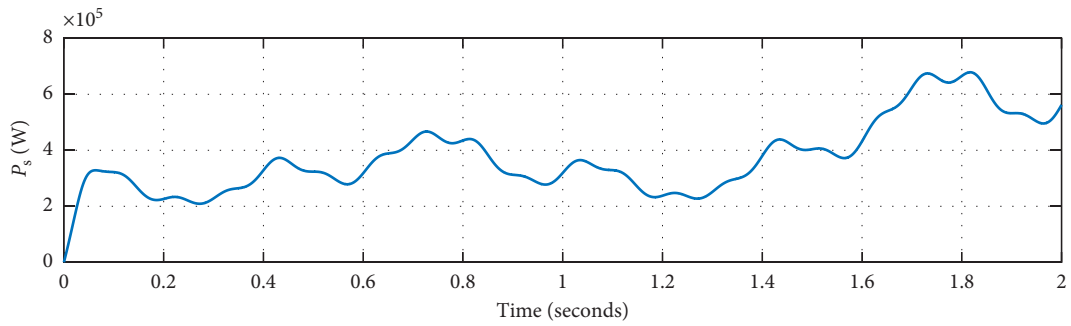


FIGURE 17: PMSG stator active power.

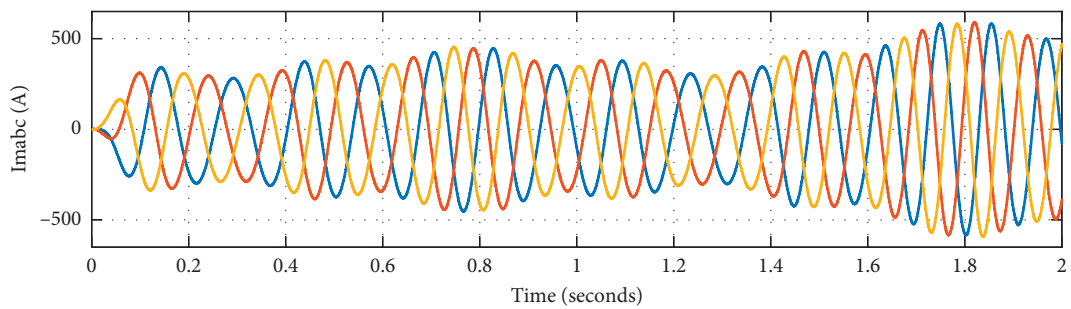


FIGURE 18: Generated stator currents.

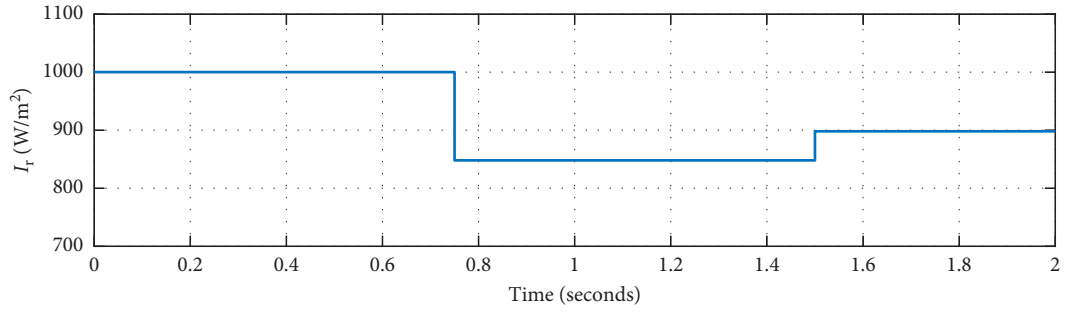


FIGURE 19: The applied irradiation profile.

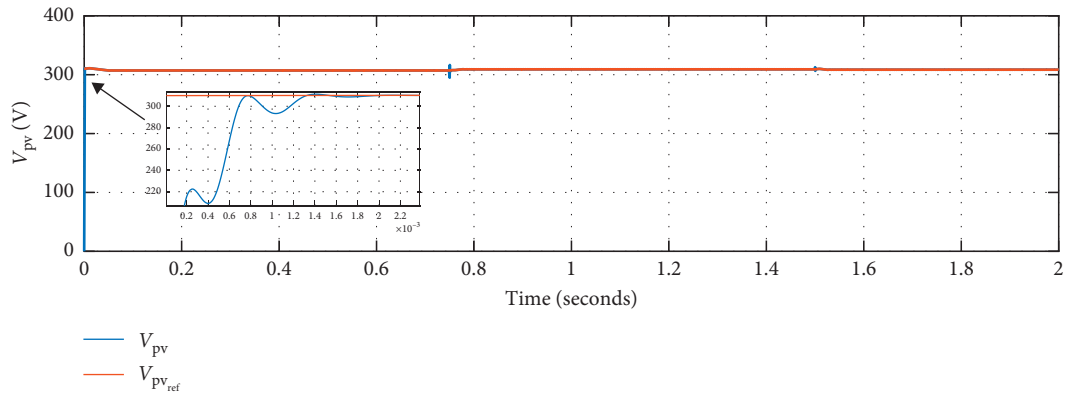


FIGURE 20: PV voltage control by ADRC.

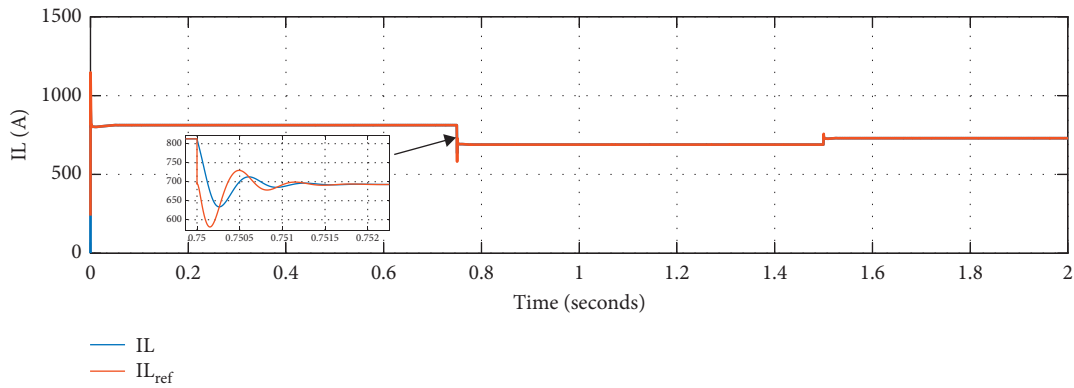


FIGURE 21: Inductor current control by ADRC.

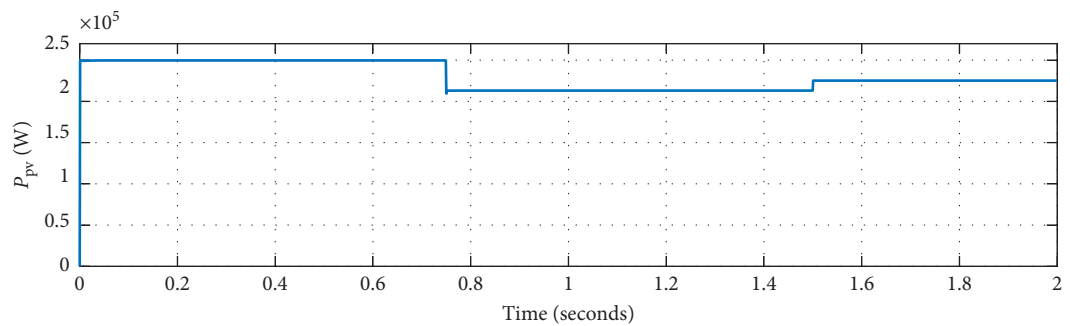


FIGURE 22: Extracted PV power by MPPT-ADRC.

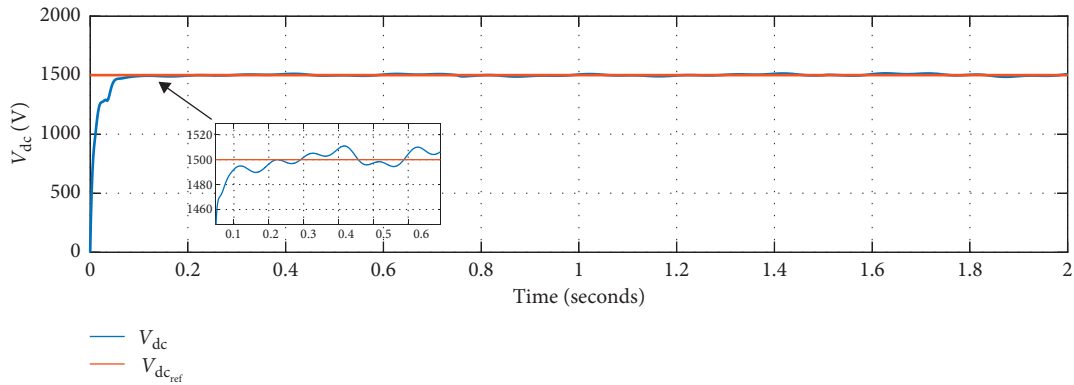


FIGURE 23: DC bus voltage control by LADRC.

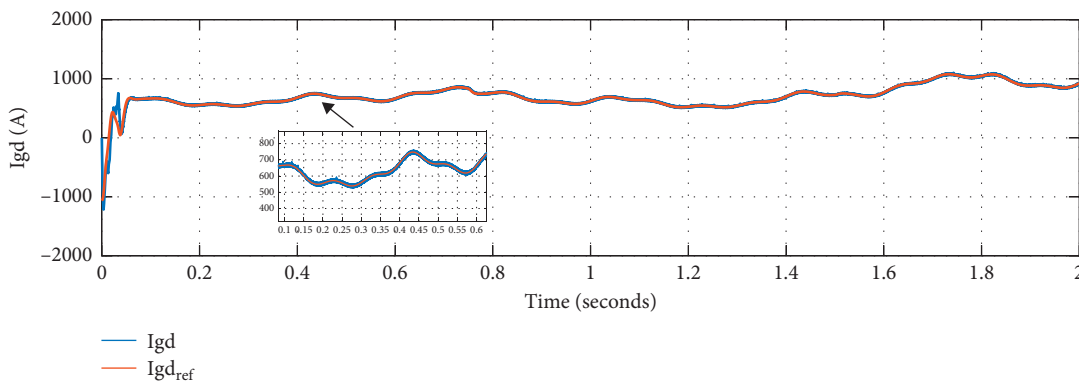


FIGURE 24: Filter direct current I_{fd} control by LADRC.

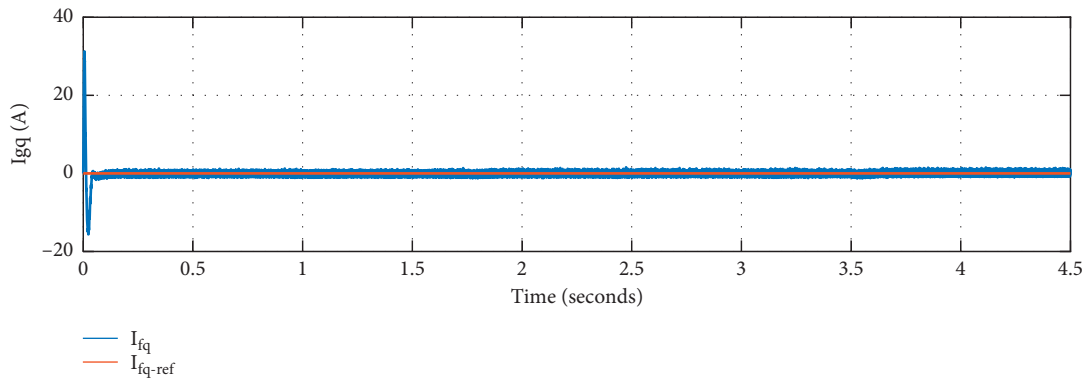


FIGURE 25: Filter quadrature current I_{fq} control by LADRC.

robustness regarding the variation of the parameters of the machine.

7.2. Discussion: Benefits and Limitations. The proposed hybrid PV-wind system presents some benefits and limitations in terms of efficiency and control, and the main advantages of the used structure are as follows:

- (i) Continuous power supply: solar and wind energies are complimentary in nature, that is, when there is no sun, there is plenty of wind and vice versa.

- (ii) Reducing cost of the system: the cost of the hybrid system is reduced because the inverter and all the associated circuits are removed.
- (iii) Reducing power loss: the converter numbers in the proposed system are less than a separated system. Therefore, the power loss of the PV's inverter is eliminated. A two-level inverter power loss is estimated to be around 0.015 pu [33]. This value is considerable in case of MW-level power plants. For the system limitations, we can mention the following:

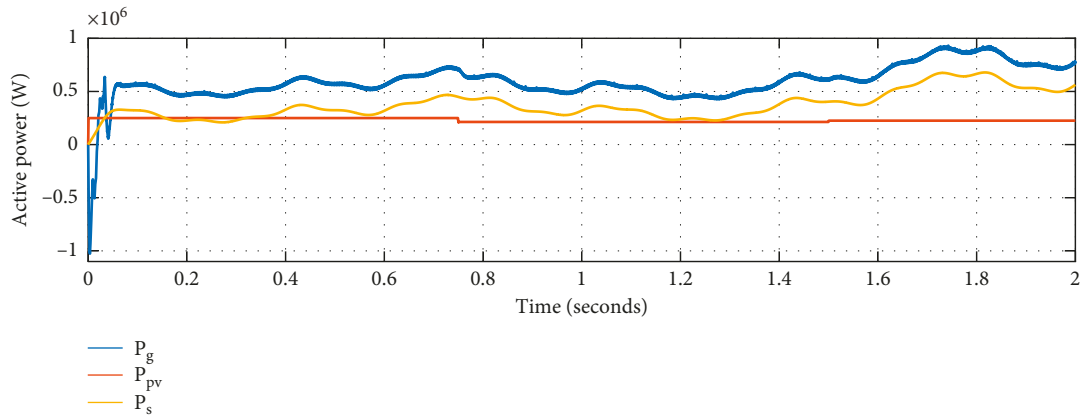


FIGURE 26: Active power injected to the grid.

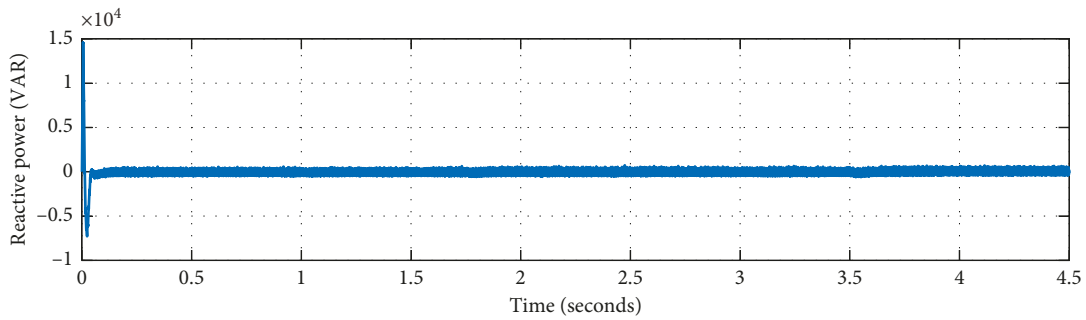


FIGURE 27: Reactive power injected to the grid.

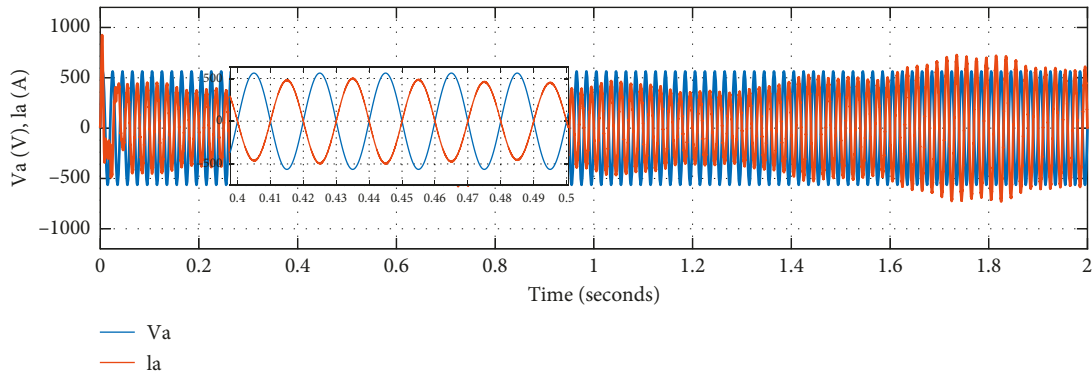


FIGURE 28: Grid voltage V_{s_a} and grid current I_{f_a} .

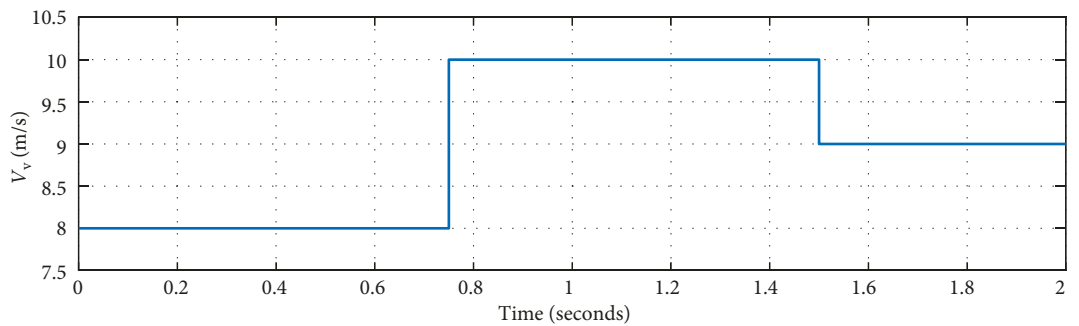


FIGURE 29: Wind speed profile.

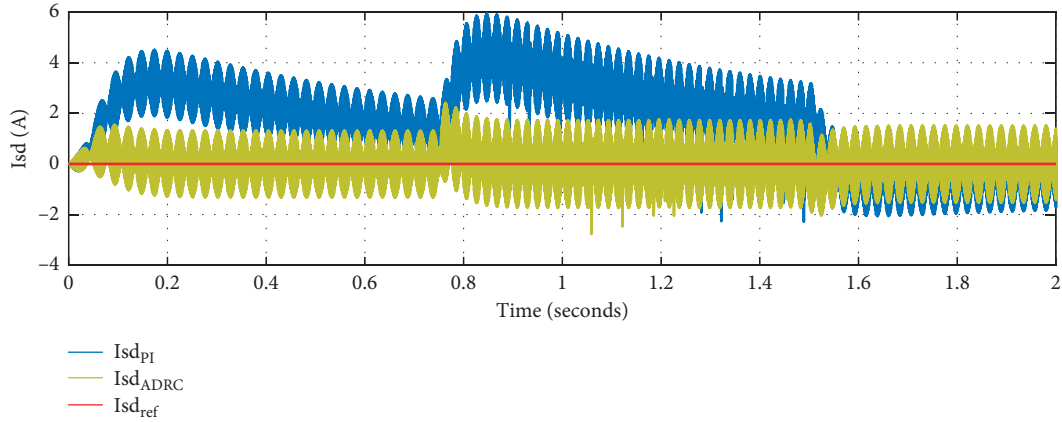


FIGURE 30: Control of d -axis stator current I_d .

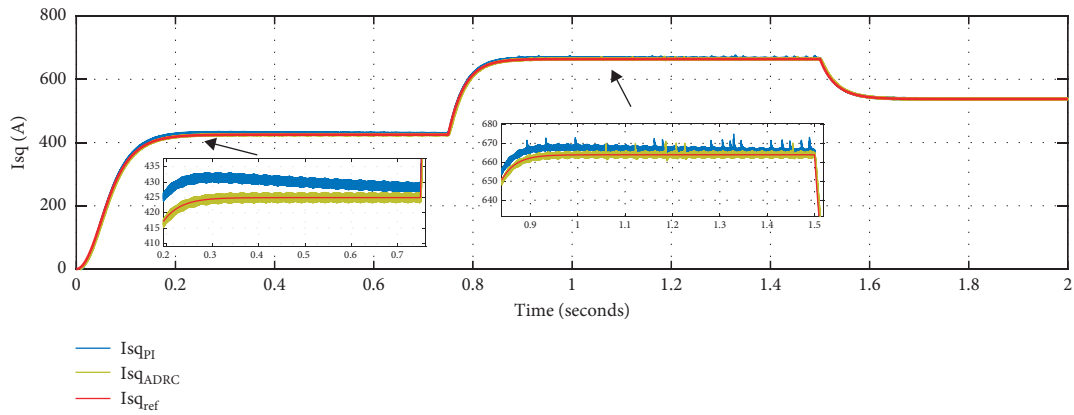


FIGURE 31: Control of q -axis stator current I_q .

- (i) Complicated controlling process: with different types of energy sources in use, the systems require some knowledge. The operation of different energy sources and their interaction and coordination must be controlled, and it can become complicated.
- (ii) Operations under grid faults: according to the new grid code, the wind power system and the PV system should not disconnect from the grid in case of voltage dips. Moreover, it is required to participate in ancillary services; therefore, the control structure needs to be adjusted.

8. Conclusion

In this article, we have studied the modeling of a hybrid energy conversion chain (wind and photovoltaic), followed by an overall control structure introducing the ADRC method and the extended state observer (ESO) which constitutes its core. Its generalized mathematical theory in the linear and nonlinear cases is discussed. It is then applied to the control of the two chains (photovoltaic and wind) in order to extract the maximum power on the one hand, and on the other hand, it is applied to the control of the grid-side converter by ensuring the stability of the DC bus voltage and

the control of the active and reactive powers exchanged with the utility grid. To prove its robustness, a simulation is established by applying variations to the machine parameters; and the test results have demonstrated that the ADRC is largely independent of its variations unlike the classical PI regulator.

Appendix

A. PMSG Wind Turbine Parameters

- (i) Radius: $R = 24$ m
- (ii) Nominal wind speed: $V_V = 12$ m/s
- (iii) Total inertia of the mechanical transmission: $J_T = 10^5$ kg·m²
- (iv) $C_{p\max} = 0.43$
- (v) $\lambda_{\text{optimal}} = 4.4971$
- (vi) Nominal power: $P_n = 750$ kW
- (vii) Stator resistance: $R_s = 6.52e^{-3}$ Ω
- (viii) Stator inductance: $L_s = L_d = L_q = 3.85e^{-3}$ H
- (ix) Flux $\Psi = 8.53$
- (x) Pair poles $P = 26$

B. PV System Parameters

- (i) PV array system rated power: $P = 250 \text{ kW}$
- (ii) PV panel rated power: $P = 255 \text{ W}$
- (iii) Open circuit voltage of the PV panel: $V_{oc} = 37.94 \text{ V}$
- (iv) Short circuit current of the PV panel: $I_{sc} = 8.76 \text{ A}$
- (v) MPP voltage of the PV panel: $V_{mpp} = 30.71$
- (vi) MPP current of the PV panel: $I_{mpp} = 8.37 \text{ A}$
- (vii) Number of series connected panels per string: $N_s = 10$
- (viii) Number of PV panel strings: $N_p = 98$

C. Grid-Side Parameters

- (i) DC bus voltage $V_{dc} = 1500 \text{ V}$
- (ii) DC bus capacitor $C = 20000e^{-6} \text{ F}$
- (iii) Filter resistance $R_f = 0.01 \Omega$
- (iv) Filter inductance $L_f = 1e^{-3} \text{ H}$

Data Availability

No data were used to support this study.

Conflicts of Interest

The authors declare that they have no conflicts of interest.

References

- [1] L. Bouselham, M. Hajji, B. Hajji, and H. Bouali, "A new MPPT-based ANN for photovoltaic system under partial shading conditions," *Energy Procedia*, vol. 111, pp. 924–933, 2017.
- [2] A. Mohapatra, B. Nayak, P. Das, and K. B. Mohanty, "A review on MPPT techniques of PV system under partial shading condition," *Renewable and Sustainable Energy Reviews*, vol. 80, pp. 854–867, 2017.
- [3] I. Abouddrar, S. E. Hani, H. Mediouni, N. Bennis, and A. Echchaachouai, "Hybrid algorithm and active filtering dedicated to the optimization and the improvement of photovoltaic system connected to grid energy quality," *International Journal of Renewable Energy Research-IJRER*, vol. 7, no. 2, 2017.
- [4] H. Yang, Z. Wei, and L. Chengzhi, "Optimal design and techno-economic analysis of a hybrid solar-wind power generation system," *Applied Energy*, vol. 86, no. 2, pp. 163–169, 2009.
- [5] M. A. Abdullah, A. H. M. Yatim, C. W. Tan, and R. Saidur, "A review of maximum power point tracking algorithms for wind energy systems," *Renewable and Sustainable Energy Reviews*, vol. 16, no. 5, pp. 3220–3227, 2012.
- [6] F. L. Tofoli, D. de Castro Pereira, and W. J. de Paula, "Comparative study of maximum power point tracking techniques for photovoltaic systems," *International Journal of Photoenergy*, vol. 2015, Article ID 812582, 10 pages, 2015.
- [7] A. E. Yaakoubi, A. Asselman, A. Djebli, and E. H. Aroudam, "A MPPT strategy based on Fuzzy control for a wind energy conversion system," *Procedia Technology*, vol. 22, pp. 697–704, 2016.
- [8] E. Rokrok, M. Shafie-khah, and J. P. S. Catalão, "Review of primary voltage and frequency control methods for inverter-based islanded microgrids with distributed generation," *Renewable and Sustainable Energy Reviews*, vol. 82, pp. 3225–3235, 2018.
- [9] S. Dhar and P. K. Dash, "Adaptive backstepping sliding mode control of a grid interactive PV-VSC system with LCL filter," *Sustainable Energy, Grids and Networks*, vol. 6, pp. 109–124, 2016.
- [10] L. Hassaine, E. Olias, J. Quintero, and V. Salas, "Overview of power inverter topologies and control structures for grid connected photovoltaic systems," *Renewable and Sustainable Energy Reviews*, vol. 30, pp. 796–807, 2014.
- [11] B. Jain, S. Jain, and R. K. Nema, "Control strategies of grid interfaced wind energy conversion system: an overview," *Renewable and Sustainable Energy Reviews*, vol. 47, pp. 983–996, 2015.
- [12] D. Nguyen and G. Fujita, "Analysis of sensorless MPPT method for hybrid PV-wind system using DFIG wind turbines," *Sustainable Energy, Grids and Networks*, vol. 5, pp. 50–57, 2016.
- [13] S. M. Tripathi, A. N. Tiwari, and D. Singh, "Optimum design of proportional-integral controllers in grid-integrated PMSG-based wind energy conversion system," *International Transactions on Electrical Energy Systems*, vol. 26, no. 5, pp. 1006–1031, 2016.
- [14] H.-W. Kim, S.-S. Kim, and H.-S. Ko, "Modeling and control of PMSG-based variable-speed wind turbine," *Electric Power Systems Research*, vol. 80, no. 1, pp. 46–52, 2010.
- [15] H. Laabidi, H. Jouini, and A. Mami, "Sliding mode control for PV-wind hybrid system connected to grid," *Environmental Engineering*, in *Proceedings of the 5th International Conference on Green Energy and Environmental Engineering (GEEE-2018)*, vol. 6, Sousse, Tunisia, April 2018.
- [16] V. N. Jayasankar and U. Vinatha, "Design of backstepping controller for PV-wind hybrid system with grid-interfacing and shunt active filtering functionality," *International Journal of Power Electronics*, vol. 9, no. 2, pp. 167–188, 2018.
- [17] J. Han, "From PID to active disturbance rejection control," *IEEE Transactions on Industrial Electronics*, vol. 56, no. 3, pp. 900–906, 2009.
- [18] S. Li and J. Li, "Output predictor-based active disturbance rejection control for a wind energy conversion system with PMSG," *IEEE Access*, vol. 5, pp. 5205–5214, 2017.
- [19] M. Arbaoui, A. Essadki, T. Nasser, and H. Chalawane, "Comparative analysis of ADRC & PI controllers used in wind turbine system driving a DFIG," *International Journal of Renewable Energy Research-IJRER*, vol. 7, no. 4, 2017.
- [20] H. Yang, Q. Jiang, and Y. Zhong, "Active-disturbance rejection control and its application to solar PV DC-DC converter," in *Proceedings of the 2010 3rd International Conference on Advanced Computer Theory and Engineering (ICACTE)*, IEEE, Chengdu, China, August 2010.
- [21] X. Yang and Y. Huang, "Capabilities of extended state observer for estimating uncertainties," in *Proceedings of the 2009 American Control Conference*, pp. 3700–3705, St. Louis, MO, USA, June 2009.
- [22] M. Hejri, H. Mokhtari, M. R. Azizian, M. Ghandhari, and L. Soder, "On the parameter extraction of a five-parameter double-diode model of photovoltaic cells and modules," *IEEE Journal of Photovoltaics*, vol. 4, no. 3, pp. 915–923, 2014.
- [23] A. Imad, S. E. Hani, A. Echchaachouai, and A. A. Energy, "Robust Active disturbance Rejection Control of a direct driven PMSG wind turbine," in *Proceedings of the 2017*

- International Renewable and Sustainable Energy Conference (IRSEC)*, pp. 1–6, Tangier, Morocco, December 2017.
- [24] A. Katkout and A. Essadki, “Nonlinear power control strategies for variable-speed wind turbines,” *International Journal of Renewable Energy Research (IJRER)*, vol. 7, no. 4, pp. 1998–2003, 2017.
- [25] A. Echchaachouai, S. E. Hani, A. Hammouch, and I. Aboudrar, “A two-level sensorless MPPT strategy using SRF-PLL on a PMSG wind energy conversion system,” *Advances in Electrical and Electronic Engineering*, vol. 15, no. 3, pp. 383–390, 2017.
- [26] H. Laghridat, A. Essadki, and T. Nasser, “Comparative analysis between PI and linear-ADRC control of a grid connected variable speed wind energy conversion system based on a squirrel cage induction generator,” *Mathematical Problems in Engineering*, vol. 2019, Article ID 8527183, 16 pages, 2019.
- [27] I. Aboudrar, S. El Hani, H. Mediouni, and A. Aghmadi, “Modeling and robust control of a grid connected direct driven PMSG wind turbine by ADRC,” *Advances in Electrical and Electronic Engineering*, vol. 16, no. 4.
- [28] G. Herbst, “A simulative study on active disturbance rejection control (ADRC) as a control tool for practitioners,” *Electronics*, vol. 2, no. 4, pp. 246–279, 2013.
- [29] S. S. Kumar, K. Jayanthi, and N. S. Kumar, “Maximum power point tracking for a PMSG based variable speed wind energy conversion system using optimal torque control,” in *Proceedings of the 2016 International Conference on Advanced Communication Control and Computing Technologies (ICACCCT)*, pp. 347–352, Ramanathapuram, India, May 2016.
- [30] A. Kihal, F. Krim, B. Talbi, A. Laib, and A. Sahli, “A robust control of two-stage grid-tied PV systems employing integral sliding mode theory,” *Energies*, vol. 11, no. 10, p. 2791, 2018.
- [31] M. H. Nehrir, C. Wang, K. Strunz et al., “A review of hybrid renewable/alternative energy systems for electric power generation: configurations, control, and applications,” *IEEE Transactions on Sustainable Energy*, vol. 2, no. 4, pp. 392–403, 2011.
- [32] S. Mishra, I. Hussain, G. Pathak, and B. Singh, “dPLL-based control of a hybrid wind-solar grid connected inverter in the distribution system,” *IET Power Electronics*, vol. 11, no. 5, pp. 952–960, 2018.
- [33] J.-I. I. Daisuke Sato, “Total loss comparison of inverter circuit topologies with interior permanent magnet synchronous motor drive system,” in *Proceedings of the 2013 IEEE ECCE Asia Downunder (ECCE)*, pp. 1–6, Melbourne, Australia, June 2013.

